Spectroscopy of alkali-metal atoms in dense supercritical ^{4}He at low temperatures

P. Moroshkin,[*] V. Lebedev, and A. Weis

Department of Physics, University of Fribourg, Chemin du Musée 3, 1700 Fribourg, Switzerland

We present an experimental study of laser-induced fluorescence spectra of Cs atoms embedded in superfluid and solid ^{4}He, as well as in dense supercritical fluid He. The studied temperature range is increased with respect to earlier studies by the use of intense laser pulses for the transient local heating of the helium sample. The analysis of the experimental spectra is based on two different approaches: the atomic-bubble model and quasistatic line-broadening theory in the limit of high perturber density. Our results indicate that the temperature dependence of the experimentally observed spectra can be traced back to temperature-dependent correlations in the motion of He atoms in the sample.

PACS number(s): 32.70.Jz, 34.10.+x, 67.10.−j, 67.25.−k

I. INTRODUCTION

The perturbation of the resonance lines of alkali-metal atoms interacting with rare-gas atoms represents a model system for atomic collisions that has been studied experimentally and theoretically for many decades. Two limiting cases for describing the effect of collisions on line parameters (shift and width) are well known: (1) perturbation due to binary or many-body atomic collisions in the gas phase (reviewed in [1]), and (2) description in terms of the so-called atomic-bubble model which applies to metal atoms embedded in superfluid and solid helium cryomatrices (reviewed in [2]). In the gas phase, the motion of rare-gas atoms is totally uncorrelated even at elevated densities and their interactions with alkali-metal atoms can be treated as independent processes. In an atomic bubble, on the other hand, the motion of the He atoms surrounding the impurity atom is strongly correlated and has to be described in terms of collective modes, such as phonons or bubble interface oscillations. Here we address the crossover between these two extreme regimes that has neither been studied experimentally nor theoretically so far.

In a dilute high-temperature gas, the spectral line shape is described by the well-known impact-broadening theory that predicts a Lorentzian profile, centered at the unperturbed transition frequency ω_0, with a width

$$\gamma = \rho_0 \int_0^\infty \sigma(v) f(v) v \, dv \qquad (1)$$

given by the rate at which binary atomic collisions occur. Here ρ_0 is the atomic density of the buffer gas, v is the collision velocity, $\sigma(v)$ is the collision cross section, and $f(v)$ is the Maxwellian velocity distribution.

This model accounts only for absorption or emission processes that occur during the time intervals between the collisions, when the atom can be considered as free. The absorption or emission during the collision can be modeled using a quasistatic approach. Normally, this contribution leads to a correction in the far wings of the line profile. For high collision rates (high densities) and in particular for slow collisions (low temperatures), the quasistatic contribution becomes significant and leads to an asymmetric line shape.

At even higher densities, one has to take many-body atomic collisions into account. The line shape becomes non-Lorentzian and shifts with respect to ω_0. When the density of atoms is so high that the absorber or emitter at any moment interacts with a large number of perturbers, the motion of the perturbers becomes unimportant and the broadening results from fluctuations of the number of perturbers located in the interaction volume that can be described by a Poissonian distribution. In that case, the line shape approaches a Gaussian profile with a spectral width γ that is proportional to $\sqrt{\rho_0}$ and a shift Δ that is a linear function of ρ_0 [1,3].

The transition from the impact regime to the many-body quasistatic regime was theoretically analyzed in [4–6] for some model interatomic potentials. It was shown that it yields a strong asymmetry of the line profile and nonlinear dependencies of γ and Δ on ρ_0. It thus provided a qualitative explanation for the experimental $\gamma(\rho_0)$ and $\Delta(\rho_0)$ dependencies for Cs–rare-gas mixtures reported in [7–9]. This series of experiments from the 1960s has explored a broad range of atomic densities, i.e., ρ_0 below 5×10^{21} cm^{-3} at rather high temperatures, $T = 400$–500 K. More recently, the topic has received renewed attention because of astrophysical applications [10–12] in the temperature range of $T = 500$–3000 K and in connection with experiments on collisional redistribution laser cooling [13,14] at $T \approx 500$ K, $\rho_0 = (1$–$6) \times 10^{21}$ cm^{-3}.

The absorption and fluorescence line profiles and the corresponding $\gamma(\rho_0)$ and $\Delta(\rho_0)$ curves for the resonance lines of Cs and Rb atoms interacting with cryogenic helium matrices were reported and reviewed in [2]. The experiments were performed at $T = 1.5$ K, with atomic He densities in the range of $(2$–$3) \times 10^{22}$ cm^{-3}. Under these conditions, helium is in the condensed (either liquid or solid) phase. The He atoms therefore do not move freely as in the gas phase, but undergo (quantum) vibrations around some fixed positions. The alkali-metal atom is located in a small spherical cavity, called atomic bubble, that is formed by repulsive alkali-metal–He forces. From a hydrodynamic model, one infers an atomic-bubble radius, R_b, of 5–7 Å [15,16]. The line shapes of the atomic absorption and emission lines calculated in the frame of such an atomic-bubble model are in good agreement with experimental spectra observed in superfluid and solid He cryomatrices. The trapping site structures and the

---

[*]Present address: Institute for Applied Physics, University of Bonn, Wegelerstrasse 8, 53115 Bonn, Germany; moroshkin@iap.uni-bonn.de

corresponding line shift and broadening for Cs and Rb atoms in liquid He were also modeled in the framework of density functional theory applied to He clusters [17,18].

The present work was motivated by observations made in our recent experiments on the photodissociation of alkali-metal dimer molecules isolated in solid He [19,20]. In that study, we found that the spectra of the fluorescence emitted by the photodissociation products are similar, but not identical, to the laser-induced fluorescence of Cs and Rb atoms in solid He. The differences in the observed line shapes were originally attributed to the fact that the two atoms produced by photodissociation remain close to each other due to the spatial confinement imposed by the matrix, and we have speculated [19,21] about the formation of a diatomic bubble. However, later experiments have revealed that the laser pulses used for the photodissociation produce a local heating of the doped solid He sample, which may lead to a softening or even a local melting of the He matrix.

Here we present a systematic study of the effect of laser heating on the spectra of Cs atoms in liquid He. Our analysis demonstrates that the local temperature of the sample can increase significantly and that the resulting fluorescence spectra are better described by quasistatic line-broadening theory than by the atomic-bubble model. The paper is organized as follows: In Sec. II, we present the experimental spectra obtained under low-power and high-power laser excitation. In Secs. III B and III C, we discuss the well-known models of line broadening and apply them to the resonance transitions of Cs that are perturbed by collisions with He. In Sec. III D, we give a short review of the atomic-bubble model and discuss its relationship with quasistatic line-broadening theory. Finally, in Sec. IV, we compare the experimental spectra with the predictions of different line-broadening models. The study of laser melting of doped solid He will be the object of a separate paper.

II. EXPERIMENT

A. Experimental setup

We have studied the laser-induced fluorescence spectra of Cs atoms embedded in liquid ^{4}He cryomatrices. A doped liquid ^{4}He matrix was produced by the technique described in the review paper [2] by Moroshkin *et al.* The sample is contained in a helium pressure cell immersed in superfluid helium, and cooled by pumping on the helium bath. The helium host matrix is doped with Cs atoms, Cs_2 molecules, and larger clusters by means of laser ablation with the second harmonic of a pulsed Nd:YAG laser focused onto a solid Cs target. The temperature is measured by means of a ruthenium oxide resistor mounted inside the pressure cell and the helium pressure is measured by a gauge installed at the warm end of the high-pressure helium filling line. Spectroscopic measurements were performed in the pressure range of 10–40 bar, and at temperatures between 1.5 and 3.5 K (experimental conditions marked in the ^{4}He phase diagram of Fig. 1). Since the implanted species quickly diffuse out of the observation region, the laser ablation is continued during the measurements.

In a first series of experiments, the $6S_{1/2}$ - $6P_{1/2}$ (D_1) and $6S_{1/2}$ - $6P_{3/2}$ (D_2) lines of Cs isolated in the He matrices were excited by near-infrared radiation of a mode-locked
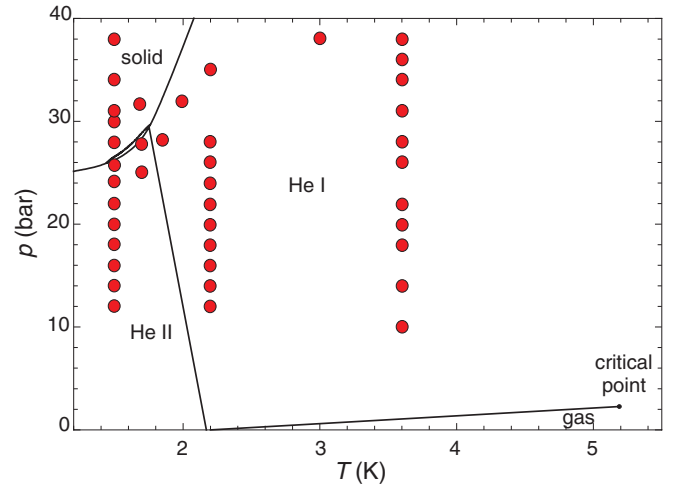

FIG. 1. (Color online) Phase diagram of ^{4}He. He I and He II denote the normal fluid and superfluid phases, respectively. The experimental conditions, under which the laser-induced fluorescence spectra were taken, are represented by solid dots.

Ti:Sapphire laser delivering a train of 100 fs ultrashort pulses at a repetition rate of 80 MHz. The laser beam enters the cryostat and the sample cell from above, via the same window that is used for laser ablation. The average laser power was kept below 10 mW (low-power excitation), thus avoiding the global heating of the sample. The laser-induced fluorescence was collected and analyzed by a grating spectrograph (0.2 nm resolution) equipped with a charge-coupled device (CCD) camera.

In a second series of experiments, we have excited Cs_2 dimer molecules that are also produced during the laser ablation process. As we have shown earlier [19,20], laser radiation can easily photodissociate these molecules into one excited and one ground-state atom, and the fluorescence of the dissociation products shows similar spectral features as laser-excited atoms. In the present experiment, we used either a pulsed (frequency-doubled) Nd:YAG laser beam ($\lambda = 532$ nm) or the radiation from a tunable optical parametric oscillator (OPO) pumped by another pulsed (frequency-tripled) Nd:YAG laser. The photodissociation-induced fluorescence spectra were recorded with the setup described above. Both laser systems work at repetition rates of 1–10 Hz and deliver pulses with typical widths of 5 ns. The mean laser power was varied in the range of 5 to 800 mW. In normal-fluid He, the heat deposited by the laser also leads to a slight increase of the steady-state temperature of the cell, while the cell filled with superfluid He is not affected and stays at the He bath temperature because of the large heat conductivity of He II. However, our temperature sensor is not sensitive to the fast rise of the *local* sample temperature immediately after the laser pulse. We will come back to this point below.

B. Fluorescence spectra under low-power excitation

Fluorescence spectra of Cs atoms in condensed He excited by low-power cw or pulsed laser radiation have been reported earlier: the Kyoto group studied Cs in superfluid He at $T = 1.6$ K [15,22], while our group presented results for Cs in bcc and hexagonal close packed (hcp) solid He at 1.6 and
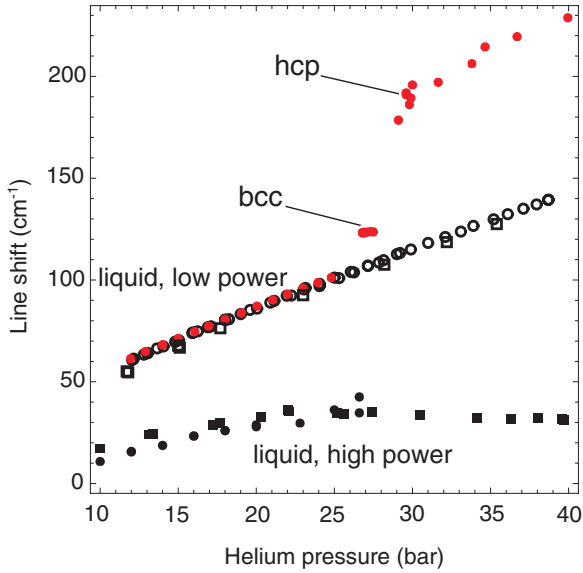
FIG. 2. (Color online) Pressure dependence of the shift of the D_1 line of Cs atoms in liquid and solid He. Filled red circles: low-power excitation at $T = 1.5$ K; empty circles: low-power excitation at $T = 2.2$ K; empty squares: low-power excitation at $T = 3.5$ K; filled squares: high-power excitation at $T = 3.5$ K; filled black circles: high-power excitation at $T = 1.7$ K.

1.5 K [16,23]. Here we report on an extension of those earlier studies to normal-fluid He at $T = 2.2$ and 3.5 K.

As discussed in [22,24,25], the Cs $6P_{3/2}$ state is strongly quenched by the formation of Cs*He$_n$ quasimolecules (exciplexes). The $6P_{1/2}$ state of Cs resides in a spherical atomic bubble and is therefore much less perturbed by the interaction with He atoms. Depending on He pressure, the D_1 spectral line is blueshifted by 50–230 cm^{-1} with respect to the free-atomic transition and broadened by 30–80 cm^{-1}. The line shape is nearly Gaussian with a slightly extended red wing. In Figs. 2 and 3, we show the observed pressure dependence of the line shift and the (FWHM) linewidth for three different temperatures. The low-power data in liquid He are not affected by temperature changes of the He matrix. The pressure dependencies of the line shifts in superfluid and normal fluid have the same linear dependence, with a slope of 2.95 cm^{-1}/bar. The line shift in solid He is larger due to the higher density and anisotropic compressibility of the solid matrix [23]. However, the linewidth data are less accurate. Above 17 bar, all data obtained in liquid He follow the same pressure dependence. At lower pressures, the linewidths measured at 3.5 K seem to be significantly larger than those at 1.5 and 2.2 K.

C. Fluorescence spectra under high-power excitation

A typical fluorescence spectrum obtained in Cs-doped liquid He under high-power pulsed Nd:YAG laser excitation is shown in Fig. 4(a). The main difference with respect to the low-power spectra is the presence of the D_2 emission line. The D_1 line is blueshifted with respect to the free-atomic transition and has a Gaussian-like line shape. The D_2 line is much weaker than the D_1 line. It is practically not shifted and has a Lorentzian-like contour with extended asymmetric
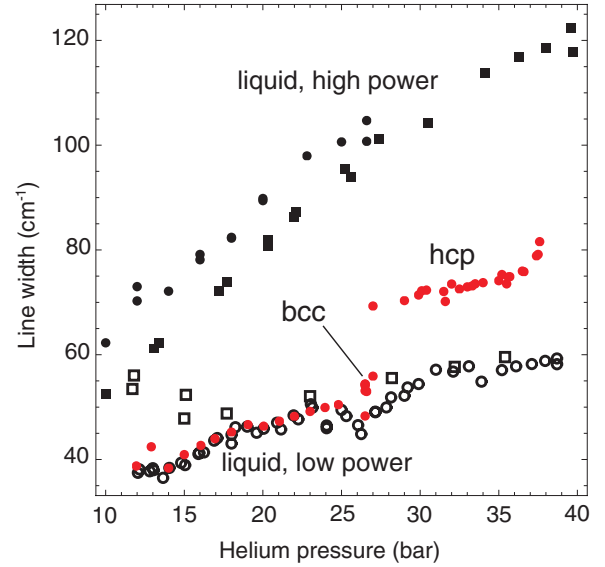

FIG. 3. (Color online) Pressure dependence of the spectral width of the D_1 line of Cs atoms in liquid and solid He. Filled red circles: low-power excitation at $T = 1.5$ K; empty circles: low-power excitation at $T = 2.2$ K; empty squares: low-power excitation at $T = 3.5$ K; filled squares: high-power excitation at $T = 3.5$ K; filled black circles: high-power excitation at $T = 1.7$ K.

wings. In Fig. 5, we show the individual line shapes of both transitions together with the corresponding Lorentzian and Gaussian fits. When increasing the He pressure, both lines broaden and the D_1 line shifts further to the blue. At the same time, the intensity of the Cs*He$_2$ exciplex emission at 950 nm (not shown in the figure) increases.

In Figs. 2 and 3, we compare the shifts and widths obtained under low-power and high-power excitation. All data points represent the results of Gaussian fits to the experimental line shapes. The statistical error bars depend on the signal magnitude, but do not exceed the size ($\approx$2 cm^{-1}) of the symbols in the figure. The D_1 line shifts obtained under high-power excitation are much smaller than the low-power line shifts in the whole investigated range of pressures and temperatures. On the other hand, the high-power linewidths are significantly larger than the low-power linewidths under the same conditions, and are even larger than the linewidths measured in solid He.

III. LINE-BROADENING THEORY

A. Interaction potentials

We model the Cs-He interaction using the *ab initio* pair potentials calculated by Pascale [26] (Fig. 6). These potentials depend on the orientation of the Cs valence electron's orbital momentum with respect to the internuclear axis, but do not account for the fine structure of the excited P states of the Cs atoms. We introduce the spin-orbit coupling by a standard method [24] and write the total Hamiltonian of the collision pair, H_{tot}, as the sum of a spin-orbit term, H_{SO}, and the interaction Hamiltonian, $H_{\text{int}}(r)$, that is diagonal in the $|L, M_L\rangle$ basis.
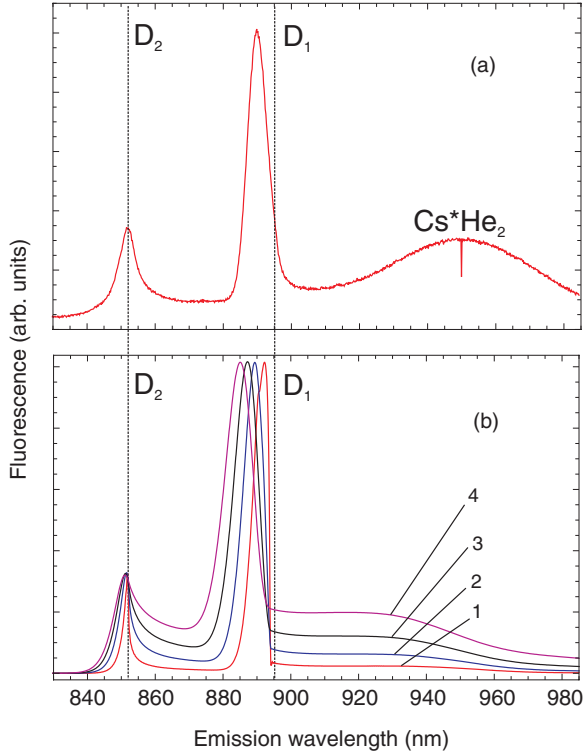
FIG. 4. (Color online) (a) Experimental laser-induced fluorescence spectrum of Cs atoms in liquid He at $T = 1.7$ K and $p = 25$ bar. Excitation by pulsed frequency-doubled Nd:YAG laser radiation (50 mW at 532 nm). (b) Calculated quasistatic line shapes of Cs resonance lines perturbed by He gas at $T = 50$ K for $p = 15$ bar (curve 1), 25 bar (curve 2), 35 bar (curve 3), and 45 bar (curve 4). The intensities of the two transitions in each spectrum are normalized to fit the corresponding ratio of the experimental peak intensities. The vertical lines mark the D_1 and D_2 transitions of the free Cs atom.

The adiabatic potential curves are obtained by a numerical diagonalization of H_{tot} (Fig. 6). The resulting eigenstates are r-dependent linear combinations of the $|L,M_L\rangle$ states. At large internuclear separations, they correspond to the $|J,M_J\rangle$ eigenstates of the free Cs atom. At small r, the interatomic interaction leads to a spin-orbit uncoupling and the eigenstates can be written as $|L,M_L\rangle$. Here, L and J denote the orbital and total angular momenta of the valence electron of the Cs atom, respectively, while M_L and M_J are their projections onto the internuclear axis.

The resulting potential $U_A(r)$ for the $J = 1/2$ fine-structure component of the $6P$ state is spherically symmetric. It has a potential well at $r \approx 3.5$ Å and a barrier at $r \approx 5$ Å. The state $J = 3/2$, on the other hand, is split into two substates, B and C, that correspond to $|M_J| = 3/2$ and $1/2$, respectively. $U_C(r)$ is repulsive at all internuclear separations, whereas $U_B(r)$ is attractive at large r with a minimum at $r \approx 3.5$ Å. All states are strongly repulsive for $r < 3$ Å. The potential $U_{P_{3/2}}$ for the $J = 3/2$ state is thus anisotropic and depends on the angle ϑ between the electronic angular momentum and the internuclear axis according to

$$U_{P_{3/2}}(r,\vartheta) = U_A(r)\cos^2\vartheta + U_B(r)\sin^2\vartheta. \qquad (2)$$
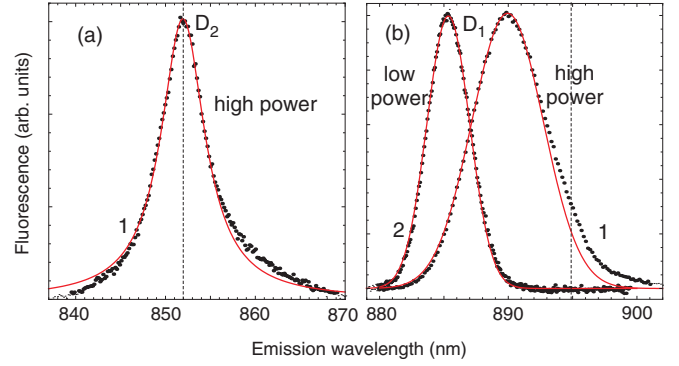

FIG. 5. (Color online) Close-up view of the experimental laser-induced fluorescence spectra of the (a) D_2 and (b) D_1 transitions of Cs in liquid He at 1.7 K and 25 bar. Dots: experimental data; solid lines: (a) Lorentzian and (b) Gaussian fits. Curve 1: high-power excitation; curve 2: low-power excitation. The D_2 line is observed only with high-power excitation. The vertical dashed lines mark the D_1 and D_2 transitions of the free Cs atom.

B. Impact-broadening calculations

In the impact regime, the broadening is due to elastic binary collisions which perturb the phase of the oscillating transition dipole moment. We have calculated the effective cross section $\sigma(v)$ for such collisions between the electronically excited Cs and He ground-state atoms using the following approach. First, we derive the classical collision trajectory $r(t)$ from a
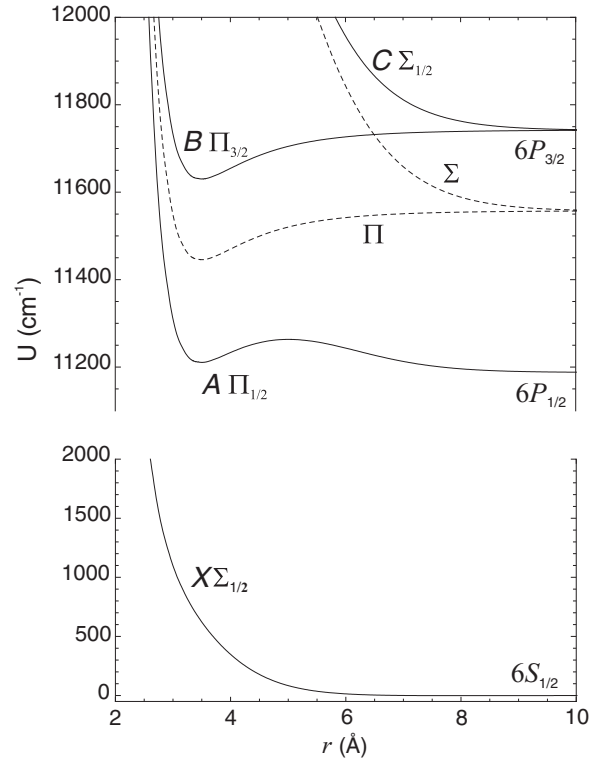

FIG. 6. Cs-He interaction potentials used in the present work. Dashed lines: *ab initio* potential curves from [26]; solid lines: potential curves including spin-orbit coupling.

numerical solution of the equation of motion,

$$\dot{r}(t) = \sqrt{\frac{2}{M}[E_0 - U_P(r(t))] - \frac{v^2 b^2}{r(t)^2}} \,. \quad (3)$$

Here, M is the reduced mass of the Cs-He pair. v and E_0 are the initial collision velocity and the corresponding kinetic energy, respectively, b is the impact parameter, and $U_P(r)$ is the Cs-He interaction potential (Sec. III A).

In a second step, we calculate the time-dependent transition frequency $\omega(t)$ and the phase

$$\phi = \int [\omega(t) - \omega_0]dt = \frac{1}{\hbar} \int \Delta U(r(t))dt \quad (4)$$

acquired by the transition dipole during the collision. Here, $\Delta U(r) = U_P(r) - U_S(r)$, where $U_S(r)$ is the ground-state Cs-He potential from [26]. We have calculated the collision phase ϕ for the relevant range of initial velocities v and impact parameters b. Only those collisions for which $\phi(b,v) \geqslant 1$ rad contribute to the line broadening [1]. The condition $\phi(b,v) = 1$ defines the largest impact parameter $b_m(v)$ that we took into account. The effective cross section $\sigma(v)$ is then given by $\sigma(v) = \pi b_m(v)^2$.

The calculations were carried out for the D_1 and D_2 lines of Cs. Due to the splitting of the $6P_{3/2}$ state (Sec. III A), there are two contributions to the D_2 cross section which we denote by σ_Π and σ_Σ. We neglect all nonadiabatic transitions between the substates and between the fine-structure components. The calculated cross sections are shown in Fig. 7.

Experiments at elevated temperatures probe mostly high-collision velocities that correspond to the relatively flat part of the $\sigma(v)$ dependence. In that case, Eq. (1) can be rewritten as $\gamma = \rho_0 \sigma \overline{v}$, with a mean velocity $\overline{v}$. The corresponding mean cross section is $\sigma \approx 150$ Å^2 for both resonance transitions of Cs. In Fig. 8, we show the values of γ/ρ_0 obtained from Eq. (1) as a function of the absolute temperature and compare them with high-temperature experimental data available in the literature [8,27–31].

The cross sections change abruptly at low velocities. For $v < 100$ m/s, the scattering from the potential barrier of the
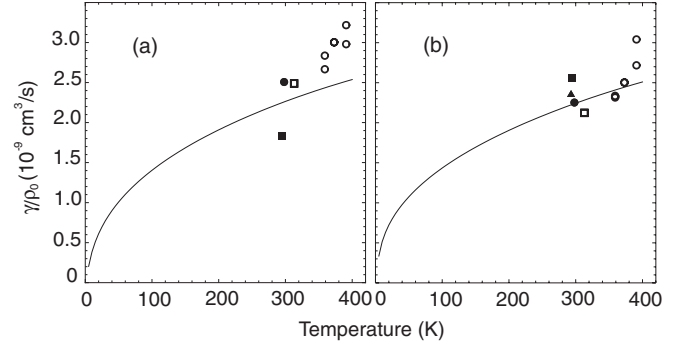
FIG. 8. Cs-He elastic collision rate γ normalized to the He atomic density ρ_0 as a function of gas temperature. Solid lines: impact-broadening calculation; symbols: experimental data for (a) D_1 and (b) D_2 transitions, respectively. Open circles: data from [8]; filled circles: data from [27]; empty squares: data from [28,29]; filled squares: data from [30]; filled triangle: data from [31].

state A, or from the repulsive state C, leaves the phase of the atomic dipole practically unchanged and therefore does not contribute to the line broadening. On the other hand, a slow collision in the state B leads to orbiting and a very large collision phase ϕ. At low temperatures, one thus expects a much larger broadening of the D_2 line.

This model also allows us to calculate the duration τ of a single collision as a function of the collision velocity and impact parameter. At low temperatures, this collision time is on the order of 1 ps, comparable to the mean time interval γ^{-1} between collisions that can be inferred from the measured Lorentzian linewidths γ. Under those conditions, the quasistatic broadening mechanism is expected to dominate the observed line shapes.

C. Quasistatic broadening calculations

In quasistatic line-broadening theory [1,32], the spectrum of the absorption (fluorescence) line is given by the Fourier transform of the atomic dipole's autocorrelation function $\Phi(s)$. When the absorber (emitter) interacts simultaneously with N perturbers, the autocorrelation function is given by

$$\Phi(s) = \left\langle \exp\left[-\frac{i}{\hbar} \sum_{k=1}^{N} \int_{t}^{t+s} \Delta U(\mathbf{r}_k(t'))dt' \right] \right\rangle_t . \quad (5)$$

Here the sum is taken over all perturbers located at positions $\mathbf{r}_k(t')$. The angle brackets denote an average over initial collision times t that can be replaced by the average over all possible initial collision geometries. With the assumption that each perturber's position is independent of all other perturbers' positions, this average can be expressed in terms of the average over positions of a single perturber:

$$\Phi(s) = \left\{ \left\langle \exp\left[-\frac{i}{\hbar} \int_{0}^{s} \Delta U(\mathbf{r}(t'))dt' \right] \right\rangle_{\text{collisions}} \right\}^N . \quad (6)$$

In the analysis of slow many-body collisions, the motion of individual He atoms around the alkali-metal atom can be neglected. In the static limit, $v = 0$, one has $\mathbf{r}(t') = \mathbf{r}$, and
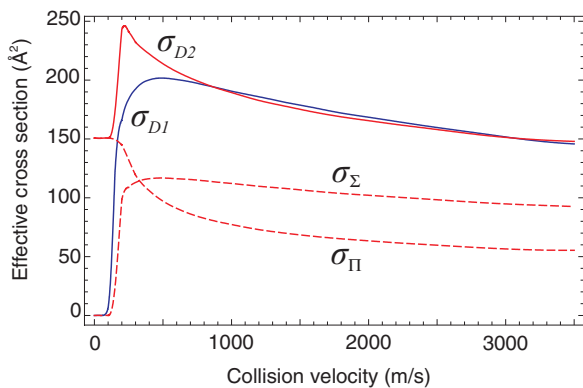

FIG. 7. (Color online) Calculated effective cross sections $\sigma_{D1}(v)$ and $\sigma_{D2}(v) = \sigma_\Sigma + \sigma_\Pi$ for elastic collisions of Cs($6P_{1/2}$) and Cs($6P_{3/2}$) atoms with He.

(6) simplifies to

$$\Phi(s) = \left\{ \left\langle \exp\left[-\frac{i}{\hbar}\Delta U(\mathbf{r})s \right] \right\rangle_{\text{collisions}} \right\}^N$$

$$= \left\{ \frac{1}{N} \int \exp\left[-\frac{i}{\hbar}\Delta U(\mathbf{r})s \right] \rho(\mathbf{r})d\mathbf{r} \right\}^N. \qquad (7)$$

The perturber density $\rho(\mathbf{r})$ describes the distribution of He atoms around the alkali-metal atom with $\int \rho(\mathbf{r})d\mathbf{r} = N$. When the number of perturbers is large and the frequency shift due to a single perturber is small, one can rewrite (7) using $(1 - \alpha)^N \simeq \exp(-N\alpha)$ as [1]

$$\Phi(s) \simeq \exp\left[-\int \left\{ 1 - \exp\left[-\frac{i}{\hbar}\Delta U(\mathbf{r})s \right] \right\} \rho(\mathbf{r})d\mathbf{r} \right]. \qquad (8)$$

In order to find $\rho(\mathbf{r})$, we consider the canonical distribution

$$\frac{1}{N}d^6N = \frac{g_p}{h^3 Q_f} \exp\left[-\frac{U_P(\mathbf{r}) + p^2/2M}{k_B T} \right] d\mathbf{r}d\mathbf{p}. \qquad (9)$$

Here, T is the absolute temperature, k_B is the Boltzmann constant, $\mathbf{p}$ is the momentum of the colliding particle, g_p is the electronic degeneracy of the P state, and Q_f is the partition function of free (unbound) He atoms defined by the normalization in the six-dimensional phase space,

$$\int_{\mathbf{p}} \int_{\mathbf{r}} d^6N = N. \qquad (10)$$

Following [33], we assume that the partition function is dominated by unbound states of He atoms far away from the alkali-metal atom, for which $U_P(\mathbf{r}) \approx 0$, so that

$$Q_f = \int\int \frac{g_p}{h^3} \exp\left[-\frac{U_P(\mathbf{r}) + p^2/2M}{k_B T} \right] d\mathbf{r}d\mathbf{p}$$

$$\approx \frac{g_p V(2\pi M k_B T)^{3/2}}{h^3} \exp\left[\frac{U_{\min}}{k_B T} \right], \qquad (11)$$

where $U_{\min}$ denotes the minimum of the potential curve $U_P(\mathbf{r})$ and V is the interaction volume. The density $\rho(\mathbf{r})$ is found by integrating (9) over $\mathbf{p}$, in the range of momenta accessible to a free particle, $p_{\min} < |\mathbf{p}| < \infty$.

For an attractive potential, $U_P(\mathbf{r}) < 0$, the minimum value of the momentum is $p_{\min}(\mathbf{r}) = \sqrt{-2MU_P(\mathbf{r})}$, whereas for a repulsive interaction, $p_{\min} = 0$, so that

$$\rho(\mathbf{r}) = \rho_0 \frac{2}{\pi} \int_{y_{\min}(\mathbf{r})}^{\infty} e^{-y} \sqrt{y}\,dy \exp\left[-\frac{U_P(\mathbf{r})}{k_B T} \right], \qquad (12)$$

where $y_{\min}(\mathbf{r}) = U_P(\mathbf{r})/k_B T$ for the attractive potential and $y_{\min}(\mathbf{r}) = 0$ for the repulsive potential curve.

For each excited state of the Cs atom, we introduce $\rho(\mathbf{r})$ defined by Eq. (12) with the corresponding cesium-helium potential $U_P(\mathbf{r})$. It is spherically symmetric for the $6P_{1/2}$ state and strongly anisotropic for the $6P_{3/2}$ state. In Fig. 9, we show typical He density profiles obtained in this way for the $6P_{1/2}$ state of Cs at $T = 20$ and 50 K. Note the local maximum of the He density at $r \approx 3.5$ Å arising from He atoms in the potential well of the A state behind the potential barrier at $r \approx 5$ Å.

We apply (8) to calculate the autocorrelation functions for the Cs-He system and obtain the corresponding fluorescence spectra by computing the Fourier transforms.
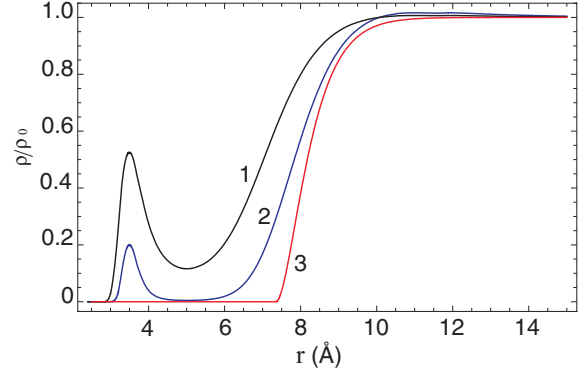

FIG. 9. (Color online) Calculated He density profiles $\rho(r)$ in the vicinity of an excited Cs ($6P_{1/2}$) atom in He gas at 50 K (curve 1), He gas at 20 K (curve 2), following Eq. (12), and superfluid He at 1.5 K, 20 bar, following Eq. (15) (curve 3).

Typical calculated fluorescence spectra of the Cs resonance doublet obtained in the static approximation at $T = 50$ K are shown in Fig. 4(b). In the experiment, the initial populations of the $6P_{1/2}$ and $6P_{3/2}$ states and the corresponding intensities of the D_1 and D_2 lines are determined by the unknown branching ratio of the photodissociation process. We therefore normalize the calculated spectra of the D_1 and D_2 lines in order to fit the characteristic ratio of their experimental peak intensities. When increasing the He pressure, the D_1 line shape approaches a Gaussian and shifts towards shorter wavelengths. Both the shift and the broadening increase with the He atomic density, as shown in Fig. 10. The abrupt increase of the linewidth and the line shift at $\rho_0 \approx 10^{21}$ cm^{-3} marks the transition from the single-perturber to a multiperturber regime. Below this point, the shift and broadening are well described by the impact model [shown in Fig. 10(b) as dashed lines]. At larger densities, we recover the well-known $\gamma \propto \sqrt{\rho_0}$ and $\Delta \propto \rho_0$ dependencies.

The D_2 line shows a much stronger perturbation than the D_1 line. The core of the line has a Lorentzian-like profile centered very close to the wavelength of the unperturbed D_2 line. On the red side of the main peak, there is an extremely broad shoulder or satellite that extends up to 950 nm. This shoulder arises from perturbers located in the potential well of the state B, close
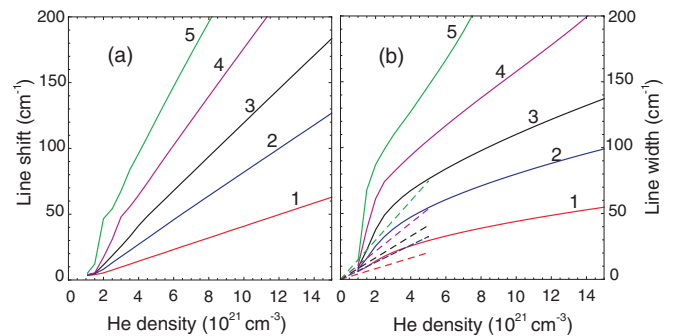

FIG. 10. (Color online) Calculated density dependence of the (a) shift and (b) (FWHM) width of the Cs D_1 line perturbed by He gas at $T = 10$ K (curve 1), 20 K (curve 2), 30 K (curve 3), 50 K (curve 4), and 100 K (curve 5). Solid lines: quasistatic model of Sec. III C; dashed lines: impact model of Sec. III B.
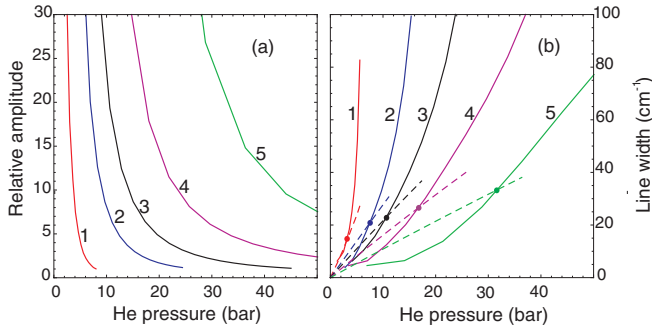
FIG. 11. (Color online) Calculated pressure dependence of the (a) relative amplitude and (b) (FWHM) width of the Cs D_2 line perturbed by He gas at $T = 10$ K (curve 1), 20 K (curve 2), 30 K (curve 3), 50 K (curve 4), and 100 K (curve 5). The relative amplitude is defined as the ratio of the D_2 peak height to the height of the saddle point at 870 nm, halfway between the D_1 and D_2 lines. Solid lines: quasistatic model of Sec. III C; dashed lines: impact model of Sec. III B.

to the Cs core. As the He density increases, the probability to find a He atom in this potential well approaches unity and the main peak disappears. As a consequence, the line shape transforms into a broad continuous spectrum similar to that of the bound-free emission from Cs*He$_2$ exciplexes. In the multiperturber regime, most of the intensity of the D_2 transition is concentrated in this red shoulder. However, a small Lorentzian-like peak at $\lambda \approx 852$ nm persists even in this regime up to $\rho_0 \approx 7 \times 10^{21}$ cm^{-3}. We believe that this shape is due to the stochastic motion of a small number (1 or 2) of He atoms in and out of the potential well of $U_B(r)$ near $r = 3$–5 Å. The D_2 line shape therefore differs from the D_1 shape that is determined by the interaction with a larger number of perturbers at $r > 6$ Å, i.e., outside the potential barrier in $U_A(r)$ of Fig. 6.

In Fig. 11(a), we show the pressure dependence of the peak amplitude of the D_2 line normalized to the height of the saddle point that is located halfway between the D_1 and D_2 lines. At low temperatures, this quantity abruptly decreases with increasing He pressure, corresponding to the disappearance of the Lorentzian-like peak discussed above. At higher temperatures, the peak is much more pronounced and persists up to higher pressures.

Figure 11(b) shows the pressure dependence of the D_2 linewidth at different temperatures. The strong temperature dependence and pressure dependence originate from the red satellite that becomes more pronounced at higher densities. In Fig. 11(b), we also show the D_2 linewidth calculated in the impact approximation. At high temperatures and moderate pressures—when the satellite is not pronounced—the impact linewidth is larger than the quasistatic width under the same conditions. The actual line shape is thus dominated by impact broadening.

D. Quasistatic line broadening in atomic bubbles

As discussed in [2,15,16], the excited $6P_{1/2}$ state of Cs resides in a spherical atomic bubble and interacts with the ≈ 30 He atoms that form the first solvation shell (bubble interface). The absorption and fluorescence line shapes of the Cs D_1 transition can thus be treated using the quasistatic

line-broadening approximation in the large perturber density limit.

The atomic bubble is similar to the distribution $\rho(r)$ of He atoms around the Cs($6P_{1/2}$) atom, introduced in Sec. III C. However, due to the confinement, i.e., the restricted motion of the densely packed He atoms at the bubble interface, the corresponding autocorrelation function $\Phi(s)$ should be calculated in a different way. In (5), we replace the average over initial collision times t by an average over atomic-bubble configurations and neglect the motion of individual He atoms, by setting $v = 0$:

$$\Phi(s) = \left\langle \exp\left[-\frac{i}{\hbar} \sum_{k=1}^{N} \Delta U(\mathbf{r}_k) s \right] \right\rangle_{\text{bubble}}. \quad (13)$$

The summation over all perturbers can be replaced by an integration over the interaction volume, which, in this case, corresponds to the He layer adjacent to the bubble boundary. Because of the spherical symmetry of the bubble, $\Phi(s)$ can be written as

$$\Phi(s) = \left\langle \exp\left[-i\frac{4\pi s}{\hbar} \int \Delta U(R)\rho(R)R^2 dR \right] \right\rangle_{\text{bubble}}. \quad (14)$$

In the previously published atomic-bubble calculations [15,16], the fluctuating distribution of He atoms around the alkali-metal atom was introduced in the following way. The helium density at the bubble interface is described by a function $\rho(R)$ that raises smoothly from $\rho(R) = 0$ inside the bubble to the bulk density $\rho(R) = \rho_0$ outside the bubble:

$$\rho(R) = 0, \quad R < R_0,$$
$$= \rho_0\{1 - [1 + \alpha(R - R_0)]e^{-\alpha(R-R_0)}\}, \quad R \geqslant R_0. \quad (15)$$

The transition region has a width of ≈ 1 Å, comparable to the characteristic delocalization distance of the He atoms in the quantum liquid (solid). This density profile is shown in Fig. 9, where it is compared to the typical density distributions in the gas phase. The bubble radius R_b is determined as the center of gravity of this interface profile.

The parameters R_0 and α are determined by the minimization of the total (i.e., atom plus bubble) energy E_{tot}:

$$E_{\text{tot}}(R_b) = E_{\text{int}}(R_b) + p\frac{4}{3}\pi R_b^3 + \kappa 4\pi R_b^2 + \frac{\hbar^2}{8m}\int \frac{\nabla\rho^2}{\rho} d\mathbf{r}. \quad (16)$$

Here, E_{int} is the energy of the Cs-He interaction, p is the hydrostatic He pressure, κ is the surface tension parameter, and m is the He atomic mass. The last term in (16) represents the volume kinetic energy arising from the localization of He atoms at the bubble interface.

The interaction energy E_{int} was derived in [15,16] from numerical solutions of the Schrödinger equation for the alkali-metal valence electron interacting with the alkali-metal core and the surrounding He atoms. In the present work, E_{int} is derived from the pair potentials between the $6P_{1/2}$ state and the He atom,

$$E_{\text{int}}(R_b) = 4\pi \int U_P(R)\rho(R)R^2 dR. \quad (17)$$

This approach allows us to compare the line shapes obtained from the atomic-bubble model to those obtained by the quasistatic calculations presented in Sec. III C.

We assume that the He atoms surrounding the atomic bubble participate in a collective motion that is represented as a superposition of breathing, quadrupole, and higher order vibration modes. In the lowest order, only the breathing vibration affects the number of perturbers in the interaction volume and therefore gives the main contribution to the line broadening. The characteristic bubble vibration frequencies ω_b obtained in the hydrodynamic model are on the order of 0.1 THz. At the temperature of 1.5 K, only the lowest vibration state of the bubble is populated and its wave function $\Psi(R_b)$ characterizes the delocalization of the bubble interface. Following [15,16], we find ω_b and $\Psi(R_b)$ by solving the one-dimensional Schrödinger equation,

$$\left[-\frac{\hbar^2}{2M_b}\frac{d^2}{dR_b^2} + E_{\text{tot}}(R_b) \right]\Psi(R_b) = E_{vib}\Psi(R_b), \quad (18)$$

with $M_b = 4\pi R_b^3 \rho_0 m$.

The average in (14) can then be calculated as

$$\Phi(s) = \int |\Psi(R_b)|^2$$
$$\times \left\{ \exp\left[-i\frac{4\pi s}{\hbar}\int \Delta U(R)\rho(R)R^2 dR \right] \right\} dR_b. \quad (19)$$

The resulting line shape closely reproduces the one reported earlier [16]. As expected, the line shift predicted by the atomic-bubble model is very close to the one predicted by the model of independent perturbers at the same He density. At the same time, the linewidth is $\approx 50\%$ smaller than the one obtained from independent perturbers of the same density.

IV. DISCUSSION

We interpret the experimentally observed fluorescence spectra by comparing them with the line shapes calculated in the impact, quasistatic, and atomic-bubble approximations. In the low-temperature limit, i.e., at low laser power, the line shape of the D_1 line is close to a Gaussian and is best described by the atomic-bubble model. Under the same conditions, the D_2 line is strongly quenched and is well described by the exciplex model [25].

When raising the laser power, the D_1 line shape remains Gaussian, while the quenching of the D_2 line gradually disappears, and a line shows up with a Lorentzian-like core that is accompanied by a strong red satellite. All of these features can be described by a quasistatic line-broadening model with independent perturbers.

A drawback of the experimental technique applied in the present work is the lack of information about the local temperature in the active part of the sample. We try to estimate the local temperature using the following considerations. As discussed in Sec. III C, the line shape of the D_1 line remains close to a Gaussian only in the multiperturber regime, i.e., at helium densities above $\rho_c \approx 10^{21}$ cm^{-3}. For temperatures above 50 K, the critical density ρ_c is reached only for $p > 10$ bar. In that case, a variation of the helium pressure (Fig. 2) would reveal a transition from the single-perturber to
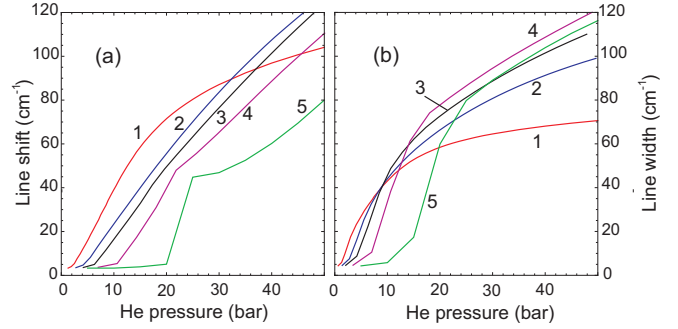

FIG. 12. (Color online) Calculated pressure dependencies of (a) the line shift and (b) the FWHM line width of the Cs D_1 line perturbed by He gas at $T = 10$ K (curve 1), 20 K (curve 2), 30 K (curve 3), 50 K (curve 4), and 100 K (curve 5).

a multiperturber regime that is accompanied by a pronounced change in the D_1 line shape. In our experiments, we could not observe such a transition, which leads us to conclude that the local temperature does not exceed 50 K. By comparing the observed amplitudes of the D_2 line with the calculated relative amplitudes of Fig. 11(a), we can estimate a lower limit of the local temperature of ≈ 20 K.

In Fig. 12, we plot the calculated quasistatic shifts and widths of the D_1 line as a function of helium pressure (same data as in Fig. 10 versus He density). In the relevant range of T and p, the D_1 line's shift and width depend only weakly on temperature at a given He pressure.

In Fig. 13, we compare the calculated widths and shifts of the D_1 line with experimental results. At low laser power, i.e., for a low local temperature, the atomic-bubble prediction yields a good agreement with experiment, while the high-power data are better described by quasistatic line broadening in a multiperturber regime with independent perturbers. The best fit to the experimental pressure dependencies is obtained by assuming a local temperature of ≈ 40 K. Our data thus suggest that the transition from the atomic bubble to the regime of independent perturbers must occur between $T = 3.5$ and $T \approx 40$ K. As discussed in Sec. III D, this transition corresponds to the crossover from the highly correlated motion
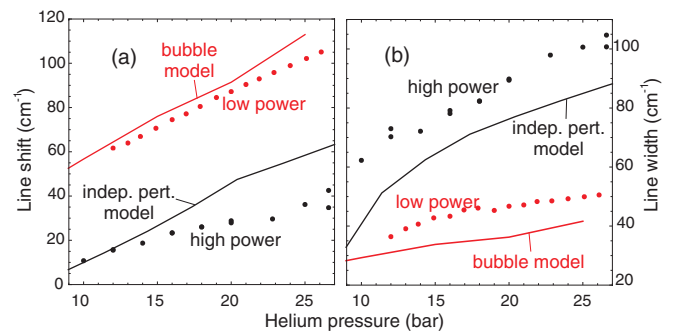

FIG. 13. (Color online) Pressure dependencies of the (a) shift and (b) (FWHM) width of the Cs D_1 fluorescence in liquid He at $T = 1.5$ K. Red circles: data from low-power excitation; black circles: data from high-power excitation; red lines: calculations based on the atomic-bubble model; black lines: calculations based on the independent perturber model, assuming a local temperature of 40 K.
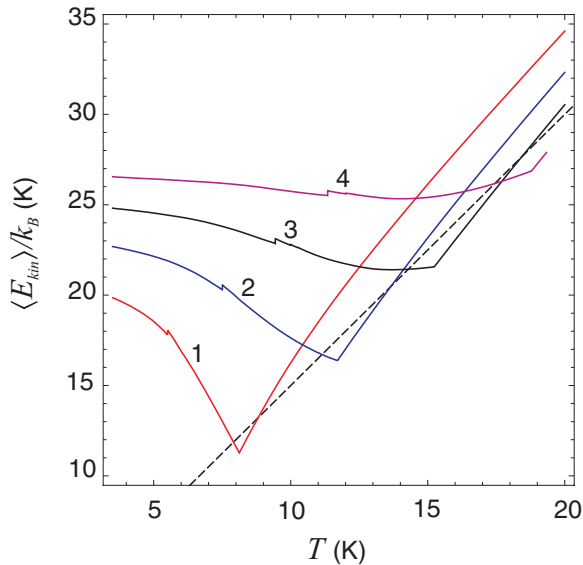
FIG. 14. (Color online) Temperature dependence of the mean kinetic energy $\langle E_{kin} \rangle$ of He atoms at $p = 10$ bar (curve 1), 20 bar (curve 2), 30 bar (curve 3), and 40 bar (curve 4). Experimental data from [34] and [35] (see the text). The dashed line represents the ideal gas law $\langle E_{kin} \rangle = 3/2 k_B T$.

of He atoms in the liquid (superfluid) phase to the uncorrelated motion of atoms in the gas phase.

There exists a vast literature (see, e.g., [36]) devoted to atomic correlations in quantum fluids, in particular in liquid ^{4}He. However, we are not aware of any treatment of the temperature dependence of correlations in a nanometer-sized system, such as an atomic bubble. In order to get an estimation of the crossover temperature, we assume a mean kinetic energy $\langle E_{kin} \rangle$ of the He atoms. It is well known that in low-temperature fluid He, $\langle E_{kin} \rangle$ is significantly larger than $3/2 k_B T$ due to a large contribution from the quantum mechanical zero-point energy ε that arises from the localization of He atoms in the condensed phase, and which therefore increases with helium density (pressure). $\langle E_{kin} \rangle$ is typically measured in deep-inelastic neutron-scattering experiments [35,37]. In the range of densities relevant for the present study, the density dependence of ε can be approximated by a linear function. Using neutron-scattering data at $T = 4.25$ K [35] to infer $\varepsilon(\rho_0)$, we obtain the total mean kinetic energy $\langle E_{kin} \rangle$ as the sum of $\varepsilon(\rho_0)$ and the internal energy $u(p,T)$, reported in [34] for a broad range of p and T values. The resulting $\langle E_{kin} \rangle(p,T)$ is plotted in Fig. 14. $\langle E_{kin} \rangle$ approaches the ideal gas value at temperatures above $T = 20$ K. Below this temperature, individual He atoms cannot be treated as independent perturbers, which is a fact that agrees well with the results of the present study.

The calculated line shapes overestimate the line shift of the D_1 line, with a discrepancy that increases with He pressure. We also find a significant disagreement in the linewidths of the D_2 line. The calculated widths are smaller than the measured ones. We suggest that this disagreement arises from the questionable assumption that the local He pressure in the active part of the sample is equal to the pressure measured by the gauge at the warm end of the filling line. It is reasonable to assume—but

difficult to model—that the strong local heating of the He matrix by the laser pulses may lead to transient changes in the local pressure and even to shock waves.

Our analysis includes only He atoms in the vicinity of, but not bound to, the Cs atoms and neglects the bound and quasibound Cs*-He states that are formed in the potential wells of the $A\Pi_{1/2}$ and $B\Pi_{3/2}$ states, which are known as exciplexes. These quasimolecular structures arising from the highly anisotropic alkali-metal–helium interaction have been analyzed in detail in [25,38–41]. The dependence of the exciplex populations on He temperature and density in the range of $\rho_0 = 10^{18}$–10^{19} cm^{-3} was studied experimentally in [38,42]. Neglecting the population of the exciplex states, especially those in the $B\Pi_{3/2}$ electronic state, leads mainly to a discrepancy between the experimental and calculated spectra in the range of 930–980 nm (see Fig. 4). It may also contribute to the discrepancies in the broadening and line shape of the D_2 line. Possible inaccuracies in the alkali-metal–helium pair potentials represent yet another source of the observed discrepancy with experiment.

V. SUMMARY

We have presented a theoretical analysis of the line shapes of the first resonance doublet of Cs perturbed by He in the impact, quasistatic, and atomic-bubble approximations. Special attention was given to the limit of high perturber densities and to the transition from a single- to a multiperturber regime. The atomic-bubble model is not applicable to the D_2 transition. On the other hand, the D_1 transition at large helium densities can be described either by the quasistatic line-broadening theory or by the atomic-bubble model. The two approaches predict very similar Gaussian line shapes that differ mostly by their spectral widths. At a fixed perturber density, the assumption of independent perturbers used in the quasistatic line-broadening theory leads to a larger broadening than that obtained in the atomic-bubble model, in which the motion of perturbers is strongly correlated.

We have carried out an experimental study of the crossover between the regime of independent perturbers (gas phase) and that of strongly correlated perturbers (condensed phase) in supercritical fluid He at low temperature. We have demonstrated that the atomic-bubble model provides a better description of the experimental spectra in the temperature range $T \leqslant 3.5$ K. The local heating of the doped He sample by intense laser pulses leads to a transition towards the regime of independent perturbers. Comparing the experimental and calculated spectra, we estimate the local temperature of the sample to be in the range of 20–50 K. The crossover between the two regimes thus occurs in a temperature range of 3.5–50 K.

[1] N. Allard and J. Kielkopf, Rev. Mod. Phys. **54**, 1103 (1982).
[2] P. Moroshkin, A. Hofer, and A. Weis, Phys. Rep. **469**, 1 (2008).
[3] W. C. Kreye, J. Quant. Spectrosc. Radiat. Transfer **107**, 154 (2007).
[4] A. Royer, Phys. Rev. A **22**, 1625 (1980).
[5] N. F. Allard and Y. G. Biraud, J. Quant. Spectrosc. Radiat. Transfer **23**, 253 (1980).
[6] D. E. Gilbert, N. F. Allard, and S. Y. Ch'en, J. Quant. Spectrosc. Radiat. Transfer **23**, 201 (1980).
[7] S. Y. Ch'en and M. Takeo, Rev. Mod. Phys. **29**, 20 (1957).
[8] R. O. Garrett and S. Y. Ch'en, Phys. Rev. **144**, 66 (1966).
[9] S. Y. Ch'en and R. O. Garret, Phys. Rev. **144**, 59 (1966).
[10] N. F. Allard and F. Spiegelman, Astron. Astrophys. **452**, 351 (2006).
[11] D. F. T. Mullamphy, G. Peach, V. Venturi, I. B. Whittingham, and S. J. Gibson, J. Phys. B **40**, 1141 (2007).
[12] K. Alioua, M. Bouledroua, A. R. Allouche, and M. Aubert-Frecon, J. Phys. B **41**, 175102 (2008).
[13] U. Vogl and M. Weitz, Nature (London) **461**, 70 (2009).
[14] U. Vogl, A. Saß, S. Haßelmann, and M. Weitz, J. Mod. Opt. **58**, 1300 (2011).
[15] T. Kinoshita, K. Fukuda, Y. Takahashi, and T. Yabuzaki, Phys. Rev. A **52**, 2707 (1995).
[16] A. Hofer, P. Moroshkin, S. Ulzega, D. Nettels, R. Müller-Siebert, and A. Weis, Phys. Rev. A **76**, 022502 (2007).
[17] T. Nakatsukasa, K. Yabana, and G. F. Bertsch, Phys. Rev. A **65**, 032512 (2002).
[18] J. Anton, P. K. Mukherjee, B. Fricke, and S. Fritzsche, J. Phys. B **40**, 2453 (2007).
[19] P. Moroshkin, A. Hofer, S. Ulzega, and A. Weis, Phys. Rev. A **74**, 032504 (2006).
[20] P. Moroshkin, A. Hofer, V. Lebedev, and A. Weis, J. Chem. Phys. **133**, 174510 (2010).
[21] A. Hofer, P. Moroshkin, D. Nettels, S. Ulzega, and A. Weis, Phys. Rev. A **74**, 032509 (2006).

[22] Y. Takahashi, K. Sano, T. Kinoshita, and T. Yabuzaki, Phys. Rev. Lett. **71**, 1035 (1993).
[23] V. Lebedev, P. Moroshkin, and A. Weis, J. Phys. Chem. A **115**, 7169 (2011).
[24] J. Dupont-Roc, Z. Phys. B **98**, 383 (1995).
[25] P. Moroshkin, A. Hofer, D. Nettels, S. Ulzega, and A. Weis, J. Chem. Phys. **124**, 024511 (2006).
[26] J. Pascale, Phys. Rev. A **28**, 632 (1983).
[27] A. Andalkar and R. B. Warrington, Phys. Rev. A **65**, 032708 (2002).
[28] G. A. Pitz, D. E. Wertepny, and G. P. Perram, Phys. Rev. A **80**, 062718 (2009).
[29] G. A. Pitz, C. D. Fox, and G. P. Perram, Phys. Rev. A **82**, 042502 (2010).
[30] E. Bernabeu and J. M. Alvarez, Phys. Rev. A **22**, 2690 (1980).
[31] Y. Inoue, K. Uchida, H. Hori, and T. Sakurai, J. Phys. Soc. Jpn. **59**, 516 (1990).
[32] P. W. Anderson, Phys. Rev. **86**, 809 (1952).
[33] R. E. M. Hedges, D. L. Drummond, and A. Gallagher, Phys. Rev. A **6**, 1519 (1972).
[34] R. W. Hill and O. V. Lounasmaa, Philos. Trans. R. Soc. A **252**, 357 (1960).
[35] K. W. Herwig, P. E. Sokol, T. R. Sosnick, W. M. Snow, and R. C. Blasdell, Phys. Rev. B **41**, 103 (1990).
[36] D. M. Ceperley, Rev. Mod. Phys. **67**, 279 (1995).
[37] D. Colognesi, C. Andreani, and R. Senesi, Europhys. Lett. **50**, 202 (2000).
[38] K. Enomoto, K. Hirano, M. Kumakura, Y. Takahashi, and T. Yabuzaki, Phys. Rev. A **66**, 042505 (2002).
[39] M. Lehner, R. Xu, and M. Jungen, J. Phys. B **38**, 1235 (2005).
[40] M. Leino, A. Viel, and R. E. Zillich, J. Chem. Phys. **129**, 184308 (2008).
[41] M. Leino, A. Viel, and R. E. Zillich, J. Chem. Phys. **134**, 024316 (2011).
[42] K. Hirano, K. Enomoto, M. Kumakura, Y. Takahashi, and T. Yabuzaki, Phys. Rev. A **68**, 012722 (2003).